Joint Special Interest Group meeting between euspen and ASPE
Advancing Precision in Additive Manufacturing
KU Leuven, Belgium, September 2023
www.euspen.eu

Dimensional accuracy of additively manufactured graded lattice structures based on X-ray microcomputed tomography

Mahmoud Osman[1,2], Fabrice Bernier[3], Priti Wanjara[2], Javad Gholipour[2], Roger Pelletier[3], Marjan Molavi-Zarandi[3], Mathieu Brochu[1]

[1] *Department of Mining and Materials Engineering, McGill University, Montréal, QC, H3A 0C5, Canada*
[2] *National Research Council Canada, Montréal, QC, H3T 1J4, Canada*
[3] *National Research Council Canada, Boucherville, QC, J4B 6Y4, Canada*

mathieu.brochu@mcgill.ca

Abstract
Recent developments in laser powder bed fusion (LPBF) additive manufacturing (AM) have enabled the fabrication of intricate, supportless, three-dimensional (3D) truss lattice structures (TLS). These geometries feature a lightweight design, high specific strength and large surface area-to-volume ratio, which makes them ideal candidates for thermal dissipation applications. However, the dimensional accuracy of TLS produced by LPBF AM decreases with complexity and the lowering of their dimensions from macro to micro-levels due to the relationship between the melt pool size, rastering and the geometry to be printed. The present study employs X-ray microcomputed tomography (µCT) to evaluate the dimensional accuracy of three different topologies of graded truss lattice structures (GTLS) produced by LPBF using stainless steel 316L powder. The unit cells of the three topologies studied for the GTLS resemble the cubic crystal system as face-centered cubic (FCC), face-centered cubic with struts in the Z-direction (FCCZ), and primitive cubic (Cubic). These lattice topologies were designed with a constant unit cell of 3 mm and varying relative densities from 0.4 to 0.8. The struts of each GTLS have been categorized with respect to their orientation with the build platform into 0°, 45° and 90° strut groups and the dimensions of each were assessed by µCT segmentation and image analysis methods. A correlation for the dimensions between each designed and fabricated strut was determined for the different strut orientations over the diameter range studied. The resulting correlations can be further applied for error compensation of the GTLS produced by LPBF AM to improve their dimensional accuracy at the micro level.

Laser Powder Bed Fusion; Stainless Steel 316L; Graded Lattice Structures; Dimensional Accuracy; X-ray Microcomputed Tomography; Strut Orientation

1. Introduction

Laser powder bed fusion (LPBF) technology has facilitated the fabrication of highly sophisticated 3D truss lattice structures (TLS) with microscale features that cannot be achieved by conventional manufacturing techniques [1]. Graded truss lattice structures (GTLS) are TLS with a graded relative density (RD) designed to equilibrate the stress distribution along the lattice in order to optimize their overall structural weight [2]. These GTLS exhibit distinct mechanical properties and energy absorption capabilities when compared to uniform TLS [3]. The performance of GTLS is highly dependent on the dimensional precision upon manufacturing to match the required strut diameter and/or the designed RD. The understanding of the dimensional variations of GTLS produced by LPBF is critical, particularly in GTLS fabricated at the microscale level with small features approaching the inherent limits of the LPBF process [4].

Multiple factors affecting the lattice dimensional accuracy have been recently studied. Rashid *et al.* [5] indicated that the scan strategy in LPBF influences the dimensional accuracy. A double scan strategy (scanning each print layer twice) promoted the overgrowth of some regions of the printed surfaces; therefore, the dimensions of ~75% of the printed surfaces were more than the CAD surfaces. Großmann *et al.* [6] investigated the effect of laser power and scan speed on the diameter of TLS produced by LPBF and concluded that increasing the laser power or scan speed increases the diameter of the struts of thin-walled lattice structures. Yan et *al.* [7] noticed that the fabricated strut size was larger than the designed value for stainless steel 316L (SS316L) gyroid lattice structures measured by µCT, where the designed strut widths of 420, 610, 790 and 920 µm deviated to 500, 700, 860 and 1,010 µm, respectively upon fabrication. A similar trend was detected by Campanelli *et al*. [8] that reported deviations in the designed strut diameter of a stochastic lattice structure made of Ti6Al4V from the nominal sizes of 500, 600 and 700 µm to 523, 626 and 725 µm, respectively upon fabrication by LPBF. Dong *et al.* [9] investigated the effect of the build orientation on the geometrical accuracy of AlSi10Mg samples produced by LPBF. In their study, dog-bone-shaped tensile struts of 1000 µm diameter were built at different orientations (35.5°, 45°, 60° and 90°) and then segmented by µCT within the gage length. The average deviation in 35.5° and 90° samples were 2.9% and -1.5%, respectively, with maximum surface roughness for 35.5° samples. The study did not address the possible variation of the dimensional deviation with changing diameter size, nor captured the deviation directly on a TLS.

In the present study, the authors evaluated the effect of the lattice topology (FCC, FCCZ, and cubic) and the strut orientation at 0°, 45° and 90° on the dimensional accuracy of their constituting struts made of SS316L by LPBF. Similar LPBF process parameters and scanning strategies were used to fabricate the three GTLS with varying RD from 0.4 to 0.8 along the build direction. The strut diameter was evaluated by direct µCT of the GTLS, which promoted the evaluation of the geometrical

deviation for a wide spectrum of strut diameters ranging from ~600 to 2500 µm; thus, a dimensional correlation between the designed and the fabricated dimensions could be achieved to be compensated in the earlier design steps.

2. Experimental Procedure

2.1. Sample Fabrication

FCC, FCCZ and Cubic GTLS were selected for the present study with a unit cell that resembles the FCC, FCC with vertical (Z direction) struts and primitive cubic crystal structures, respectively. The GTLS were modelled using SolidWorks® 2021, each of the GTLS comprised 5 × 5 × 5 periodic unit cells with a constant cell length (C_l) of 3 mm for all models. The strut diameter of each GTLS varied to achieve a graded RD along the build direction of 0.8, 0.7, 0.6, 0.5 and 0.4, for the five layers respectively from the build plate to the top layer.

The SS316L powder used in the present work was supplied by Renishaw plc. Table 1 presents the chemical composition of the sourced powder. The particle size distribution (PSD) was measured using a Horiba laser scattering particle size analyser LA-920 (Kyoto, Japan) and resulted in D10, D50 and D90 of 20, 29 and 45 µm, respectively.

Table 1. The chemical composition of the SS316L powder (wt%)

Fe	Cr	Ni	Mo	Mn	Si	C	N
Balance	17.7	12.6	2.3	1.1	0.62	0.02	0.09

The Renishaw AM250 (Renishaw, Wotton-under-Edge, UK) LPBF machine was used to build the GTLS coupons. The machine is equipped with 200 W laser power and a 70 µm focal diameter. Standard laser power for SS316L was adopted, resulting in a volumetric energy density of 106 J/mm^3. The samples were then cut from the build plate with an abrasive cutter. Fig. 1 displays a 3D view of the fabricated GTLS and their corresponding designed unit cells. The colour of the struts in each unit cell indicates their orientation, where red, orange and green struts refer to 0°, 45° and 90°, respectively. In the present study, we measured 0° and 45° struts of the FCC GTLS, 0°, 45° and 90° struts of the FCCZ GTLS and 90° struts of the Cubic GTLS.

2.2. Sample characterization

µCT was undertaken on the GTLS using a Nikon HMXST 225 system (Brighton, MI, USA) equipped with a Perkin-Elmer 1621AN CsI (2000 × 2000 pixels, 40 × 40 cm^2 and 200 µm/pixel) detector panel. The X-ray µCT system was operated at a voltage of 175 kV, a current of 130 µA with a 0.25 mm Ag filter, and an exposure time of 1 s. Four frames per projection were taken and a voxel size of (13 µm)^3 was used. The data was imported to CT Pro 3D version XT 3.1.12 to obtain 3D reconstructed topographies of the GTLS to analyse the geometrical imperfections of their constituting struts. The Object Research System (ORS) Dragonfly software version 2021.1 was then used for lattice segmentation and imaging of the strut cross-section. Upper Otsu threshold was used to distinguish the strut cross-section from the entrapped powder within the GTLS. Fig. 2 demonstrates the methodology adopted for the cross-sectional acquisition of struts oriented at different angles (0°, 45° and 90°). The white section lines represent the planes at which GTLS was sectioned to obtain their actual cross-section. Five layers were taken at each section line to obtain a wide range of data points for each strut size. Finally, ImageJ software was used to calculate the fitted diameter from the highlighted cross-section image obtained from Dragonfly and the deviation of the build (e) from the CAD diameter was calculated accordingly. Similar methodology was employed for imaging the struts of FCC and Cubic GTLS.

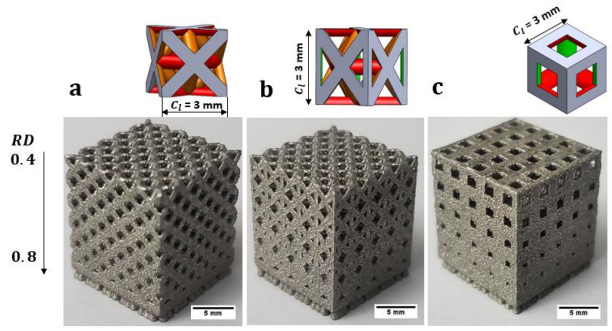

Figure 1. A 3D view of the fabricated GTLS and their corresponding unit cells (a) FCC, (b) FCCZ and (c) Cubic

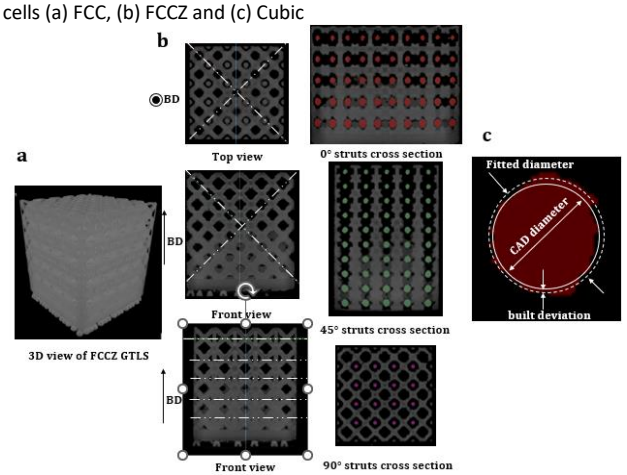

Figure 2. (a) A 3D view of the µCT FCCZ GTLS, (b) the acquisition of struts cross-section for different orientations (0°, 45° and 90°) and (c) the calculation of the build deviation.

3. Results and discussion

3.1. Effect of the strut orientation on the strut dimensional accuracy

Table 2 shows the CAD and measured strut diameters of the FCCZ GTLS for the three different orientations, namely 0°, 45° and 90° of each lattice layer. The results indicate that the 45°struts exhibited the highest relative error (RE) among the strut orientations studied; specifically, RE ranged between 15 and 5% as the designed diameter increased from 618 to 1031 µm. The negative correlation between the strut diameter and the RE can be attributed to the constant deviation (e) between the CAD and measured average diameter for the studied diameter range (~600-1000 µm), which yields a more pronounced RE for smaller struts. A similar trend was observed for the 0° struts, while showing a RE between 10 and 5% as the nominal diameter increased from 618 to 1031 µm. Lower RE were observed for 90° struts ranging between 4 and -2% for diameters of 618 and 1031 µm, respectively.

The higher deviation from the CAD diameter in the 45° struts can be attributed to the over-melting of the lower side of the inclined struts. This has been further explained by Dong *et al*. [9] through finite element modelling (FEM) of the thermal transfer history in the LPBF process of AlSi10Mg struts at different orientations. Their FEM results showed different temperature gradients with the different build orientations, where the maximum temperature on the strut constituted larger volume of the inclined struts and decreased gradually with increasing build inclination from 35.5° to 90°. Fig. 3 shows a schematic of the maximum temperature location during LPBF of 45° and 90° struts as plotted in [9]. This implies an over-melting of the 45° struts at the downside of the strut and higher expected RE compared to 90° struts.

The presented mechanism can be further applied to 0° struts since the tangent to the circle has a variable build angle (θ) as the LPBF process progresses. Figure 4a depicts a schematic of the build angle of a horizontal strut as a function of the build height (H) and the strut radius (R) as follows:

$$\theta = \sin^{-1}\left(\frac{\sqrt{2HR - H^2}}{R}\right), \quad 0 \leq H \leq 2R$$

The build angle θ varies from 0° at H= 0 and increases with the build height to 45° at H = ~0.29 R, then increases further to 90° when H = R. An inverse trend takes place for the upper half of the strut ($R \leq H \leq 2R$), where θ decreases gradually from 90° back to 0°. Fig. 4b shows the expected horizontal strut cross-section compared to the CAD diameter. The deviation is expected to be more pronounced at the bottom of the strut where θ~0°; then it is expected to decrease gradually until the half of the stut where θ~90°. Fig 4c shows a measured cross-section exhibiting a similar deviation from the CAD diameter as expected.

3.2. Effect of the lattice topology on the strut dimensional accuracy

Table 3 presents the CAD and measured strut diameters of the FCC and Cubic geometries for the different strut orientations. Comparing the RE in 0° struts in both FCCZ (Table 2) and FCC (Table 3), it can be observed that the RE is statistically similar in both lattices at 95% confidence interval. A similar trend can be observed for the 45° struts, which indicates that the RE in both 0° and 45° struts were independent on the lattice topology, in particular FCC and FCCZ lattice topologies. This can be explained based on the previous observations where the deviation from the CAD dimensions was mainly attributed to thermal history on the strut and possible overgrowth due to over-melting. In the FCCZ GTLS, the 0° and 45° struts were not in direct contact with the vertical struts; thus, the thermal history on them will resemble that of the FCC lattice and a significant RE change between both lattices is not expected.

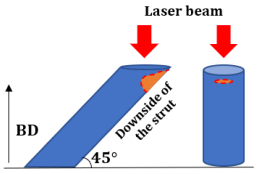

Figure 3. A schematic of the maximum temperature location in 45° and 90° struts in a LPBF process, adopted from [9]

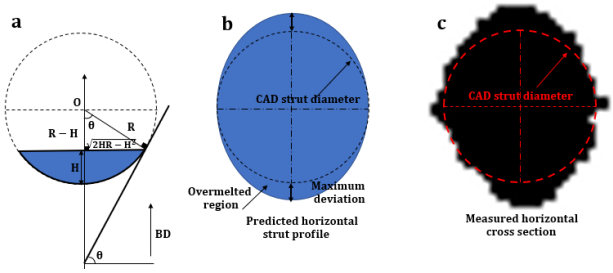

Figure 4. Deviation in horizontally built struts from CAD dimensions: (a) a schematic of the build angle with the build height, (b) predicted and CAD cross-section and (c) µCT measured cross-section against CAD dimensions.

3.3. A correlation between the measured and CAD diameter for the different strut orientations

Fig. 5 and 6 show the correlation between the measured average diameter and the CAD diameter of the 0° and 45° struts, respectively. The data points perfectly fit a linear relation with a coefficient of determination (R^2> 0.99) for both FCC and FCCZ struts. The linear relations of the FCC and FCCZ struts are interchangeable since the lattice topology did not significantly affect the deviation with the CAD dimensions, as discussed earlier. Fig. 7 compares the linearly fit data of the measured 90° struts and their corresponding CAD diameter for FCCZ and Cubic GTLS. The prediction of the linear model of FCCZ 90° in the range of (618 – 1031 µm) deviates more from that of the Cubic 90° of the range (1510 – 2510 µm) as the diameter increases. Therefore, the linear model of FCCZ can be used to predict the fabricated 90° struts diameter in the range of 600 – 1500 µm, while the cubic model can be used for struts in the range of 1500 – 2500 µm.

Table 2. CAD and measured diameters of the constitutive struts of the FCCZ GTLS at the different orientations and the corresponding build deviation (e) and relative error (RE) at 95% confidence interval

Layer RD	CAD Dia. (µm)	0° struts			45° struts			90° struts		
		Measured Dia. (µm)	e	RE (%)	Measured Dia. (µm)	e	RE (%)	Measured Dia. (µm)	e	RE (%)
L40	618	691 ± 32	73	10 ± 2	709 ± 22	91	15 ± 1	643 ± 9	25	4 ± 1
L50	715	789 ± 26	74	9 ± 2	803 ± 16	88	12 ± 1	744 ± 14	29	4 ± 1
L60	813	893 ± 28	80	9 ± 1	897 ± 27	84	10 ± 1	834 ± 19	21	3 ± 1
L70	916	990 ± 27	74	8 ± 1	960 ± 29	44	5 ± 1	909 ± 18	-7	-1 ± 1
L80	1031	1085 ± 37	54	5 ± 2	1087 ± 25	56	5 ± 1	1007 ± 15	-24	-2 ± 1

Table 3. CAD and measured diameters of the constitutive struts of the FCC and Cubic GTLS at the different strut orientations and the corresponding deviation (e) and relative error (RE) at 95% confidence interval

Layer RD	FCC GTLS							Cubic GTLS			
	CAD Dia. (µm)	0° struts			45° struts			CAD Dia. (µm)	90° struts		
		Measured Dia. (µm)	e	RE (%)	Measured Dia. (µm)	e	RE (%)		Measured Dia. (µm)	e	RE (%)
L40	638	738 ± 32	100	16 ± 2	720 ± 17	82	13 ± 1	1510	1521 ± 15	11	1 ± 0
L50	740	834 ± 31	94	13 ± 2	807 ± 27	67	9 ± 1	1750	1772 ± 10	22	1 ± 0
L60	840	909 ± 30	69	8 ± 2	898 ± 33	58	7 ± 1	1990	2009 ± 10	19	1 ± 0
L70	948	1036 ± 27	88	9 ± 1	976 ± 29	28	3 ± 1	2240	2255 ± 9	15	1 ± 0
L80	1071	1149 ± 34	78	7 ± 1	1103 ± 33	32	3 ± 1	2510	2537 ± 11	27	1 ± 0

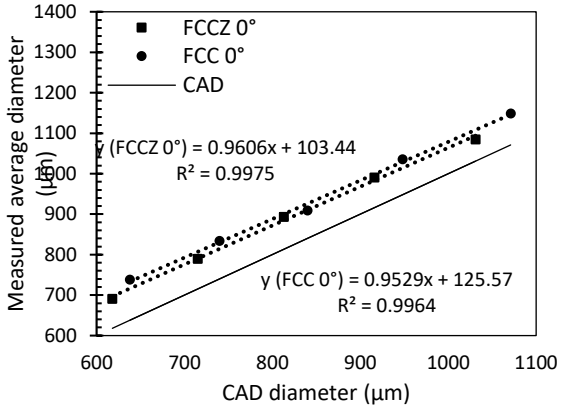

Figure 5. A correlation between measured and CAD strut diameter built at 0° from the horizontal in FCC and FCCCZ GTLS

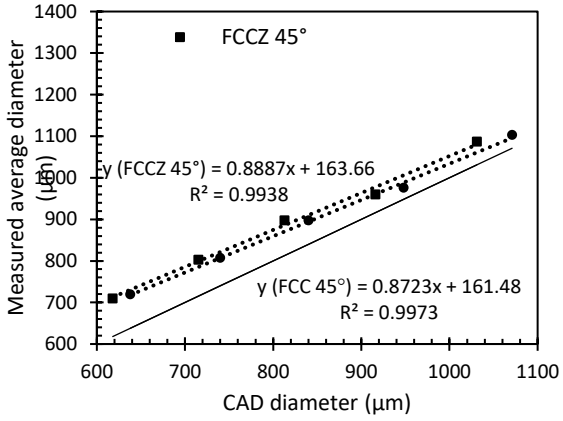

Figure 6. A correlation between measured and CAD strut diameter built at 45° from the horizontal in FCC and FCCCZ GTLS

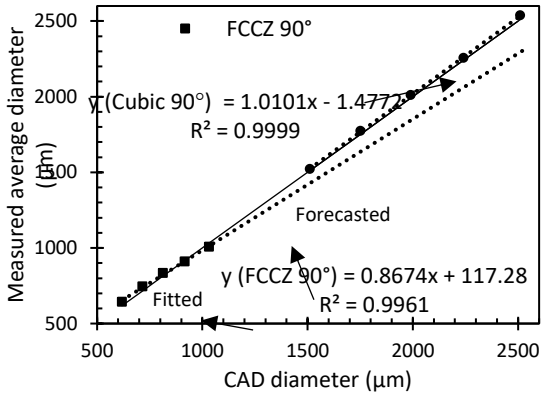

Figure 7. A correlation between measured and CAD strut diameter built at 0° from the horizontal in FCCZ and Cubic GTLS

4. Conclusions

In this study, the dimensional accuracy of SS316L FCC, FCCZ and Cubic GTLS produced by LPBF was assessed using µCT. The effect of the strut build orientation (0°, 45° and 90° with the horizontal) and the printed lattice topology on the strut dimensional accuracy were addressed. In FCCZ GTLS, 0° struts showed a RE of 10 ± 2% for ~600 µm struts and decreased to 5 ± 2% for ~1000 µm struts at 95% confidence level. While 45° struts showed a RE of 15 ± 1% and 5 ± 2% for ~600 and 1000 µm struts, respectively. 90° struts exhibited the least RE of 4 ± 1% and 1 ± 0% for ~600 and 1000 µm struts, respectively, and less than 1% for ~1500 – 2500 µm diameter range. Statistically similar RE values were obtained for FCC and FCCZ GTLS having 0° and 45° struts indicating the insignificance of the lattice topology on dimensional accuracy of the built struts. A correlation between the fabricated and designed strut diameter was linearly fitted with $R^2 > 0.99$. The linear fitting of the measured strut diameter (y) as a function of the CAD diameter (x) in µm is given by $y_{FCCZ0°} = 0.96\,x + 103$ and $y_{FCCZ45°} = 0.89\,x + 163$, where x is in the range of 618 – 1031 µm. For 90° struts, the linear relation $y_{FCCZ90°} = 0.87\,x + 117$ can be applied in the range of 600 – 1500 µm, while $y_{Cubic90°} = 1.01\,x - 1.48$ can be applied for the range of 1500 – 2500 µm.

The methodology presented provides a fully representative analysis method of µCTed GTLS to assess the deviation between the CAD and fabricated diameter for different struts of variable sizes along the GTLS. However, µCT of the entire lattice limits the maximum achievable resolution, which was 13 µm in this study. For higher accuracy in diameter measurements, a smaller specimen volume must be scanned. It is crucial to consider the deviation from the CAD diameter after LPBF, particularly in struts less than 1000 µm whether built horizontally or inclined at 45° since the RE can be as high as 15% due to the different thermal history across the cross-section during LPBF.

In future work, the correlations between the designed and fabricated diameter will be utilized in error compensation schemes to modify the designed diameter of the strut according to its orientation to improve their dimensional accuracy. In addition, the influence of the strut build orientation on the strut profile will be further investigated through high resolution µCT images of one unit cell of the lattice, which will help understand the underlying deviation mechanism using FEM.

Acknowledgement

This work was conducted as part of a project funded by the National Research Council Canada's (NRC) METALTec industrial research group, as well as the Natural Sciences and Engineering Research Council of Canada (NSERC) under grant number (CRDPJ 538319-18) and the Centre Quebecois de recherche et de developpement de l'aluminium (CQRDA).

References

[1] M. G. Rashed, M. Ashraf, R. A. W. Mines, and P. J. Hazell, "Metallic microlattice materials: A current state of the art on manufacturing, mechanical properties and applications," *Mater. Des.*, vol. **95**, pp. 518–533, 2016.

[2] L. Bai, C. Yi, X. Chen, and Y. Sun, "Effective Design of the Graded Strut of BCC Lattice," *Materials (Basel).*, vol. **12**, no. 13, 2192, 2019.

[3] D. S. J. Al-Saedi, S. H. Masood, M. Faizan-Ur-Rab, A. Alomarah, and P. Ponnusamy, "Mechanical properties and energy absorption capability of functionally graded F2BCC lattice fabricated by SLM," *Mater. Des.*, vol. **144**, no. 2017, pp. 32–44, 2018.

[4] C. López-García, E. García-López, H. R. Siller, J. A. Sandoval-Robles, and C. A. Rodriguez, "A dimensional assessment of small features and lattice structures manufactured by laser powder bed fusion," *Prog. Addit. Manuf.*, vol. **7**, no. 4, pp. 751–763, 2022.

[5] R. Rashid, S. H. Masood, D. Ruan, S. Palanisamy, R. A. Rahman Rashid, and M. Brandt, "Effect of scan strategy on density and metallurgical properties of 17-4PH parts printed by Selective Laser Melting (SLM)," *J. Mater. Process. Technol.*, vol. **249**, pp. 502–511, 2017.

[6] A. Großmann, J. Felger, T. Frölich, J. Gosmann, and C. Mittelstedt, "Melt pool controlled laser powder bed fusion for customised low-density lattice structures," *Mater. Des.*, vol. **181**, p. 108054, 2019.

[7] C. Yan, L. Hao, A. Hussein, P. Young, and D. Raymont, "Advanced lightweight 316L stainless steel cellular lattice structures fabricated via selective laser melting," *Mater. Des.*, vol. **55**, pp. 533–541, 2014.

[8] S. L. Campanelli, N. Contuzzi, A. D. Ludovico, F. Caiazzo, F. Cardaropoli, and V. Sergi, "Manufacturing and characterization of Ti6Al4V lattice components manufactured by selective laser melting," *Materials (Basel).*, vol. **7**, no. 6, pp. 4803–4822, 2014.

[9] Z. Dong, Y. Liu, W. Li, and J. Liang, "Orientation dependency for microstructure, geometric accuracy and mechanical properties of selective laser melting AlSi10Mg lattices," *J. Alloys Compd.*, vol. **791**, pp. 490–500, 2019.